Comparative Study of OpenFOAM Solvers on Separation Pattern and Separation Pattern Transition in Overexpanded Single Expansion Ramp Nozzle

T. Yu[1,2], Y. Yu[1,2,3†], Y. P. Mao[2], Y. L. Yang[1,2] and S. L. Xu [2]

[1] *School of Aeronautics, Chongqing Jiaotong University, 400074, Chongqing, China*
[2] *The Green Aerotechnics Research Institute of Chongqing Jiaotong University, Chongqing Key Laboratory of Green Aviation energy and power, 401120, Chongqing, China*
[3] *Nanjing University of Aeronautics and Astronautics, Jiangsu Province Key Laboratory of Aerospace Power System, 210016, Nanjing, China*

†*Corresponding Author Email: yuyang227@vip.sina.com*

ABSTRACT

Flow separation in overexpanded single expansion ramp nozzles (SERN) involves complex phenomena, such as shock waves, expansion waves, turbulent boundary layers, and shear layers. Computational fluid dynamics plays a crucial role in studying unsteady flow behaviour in supersonic nozzles, allowing for an investigation into the dynamic flow field characteristics. However, the application of OpenFOAM as a numerical tool for studying SERN in the field of compressible flows, particularly in the overexpansion state where the flow field characteristics are more complex, has received relatively less attention. In this study, the flow field characteristics of an overexpanded SERN under different turbulence models are investigated through a combination of experiments and numerical calculations. The qualitative and quantitative predictive performance of two compressible flow solvers in OpenFOAM, namely, rhoCentralFOAM and sonicFOAM, are compared in terms of flow separation pattern and separation pattern transitions within the overexpanded SERN. The ability of rhoCentralFOAM and sonicFOAM to accurately predict complex flow states is evaluated. Results indicate that the numerical simulations conducted using rhoCentralFOAM and sonicFOAM successfully capture flow separation, separated shock waves, separated bubbles and shear layers for two types of restricted shock separation patterns at the same nozzle pressure ratio (*NPR*), demonstrating agreement with experimental results. However, sonicFOAM initiates the transition in the separation pattern 0.0773 *NPR* earlier than rhoCentralFOAM during the whole separation pattern transition process of the SERN. The transition process in sonicFOAM lasts longer and exhibits a greater variation in *NPR*. SonicFOAM fails to accurately predict certain aspects, such as the pressure rise after the separation bubble, the reattachment shock wave, and tends to overestimat the length of the separation shock length. Consequently, sonicFOAM cannot be recommended as a suitable solver for accurately capturing the separation pattern of an overexpanded nozzle.

1. INTRODUCTION

The nozzle is a critical component of airbreathing hypersonic propulsion systems, directly influencing the flight performance of the entire system. Studies have revealed that the nozzle accounts for approximately 70% of the thrust when the flight Mach number (*Ma*) is 6 (Edwards et al., 1975), and a 1% decrease in the nozzle thrust coefficient leads to a 4% loss in overall thrust (Lederer & Krueger, 1993). Given the high Mach numbers involved, the working nozzle pressure ratio is usually higher. The rear body of the vehicle is typically used as the expansion surface, forming a single expansion ramp nozzle (SERN) (Zhou & Wang, 2019), to facilitate integrated vehicle and nozzle installation.

When the outlet pressure of the SERN falls below the ambient pressure, it operates in an overexpanded condition. To attain pressure equilibrium with the surrounding conditions, an oblique shock wave is produced inside the nozzle, leading to a flow field characterized by shock waves, expansion waves, turbulent boundary layers, and shear layers. This leads to considerable flow losses and deterioration in nozzle performance. The overexpansion state of the nozzle can profoundly affect the performance, service life of the nozzle (Hemmati & Namazian, 2021; Mirjalily, 2023) and the flight safety of the vehicle (Yu et al., 2014b).
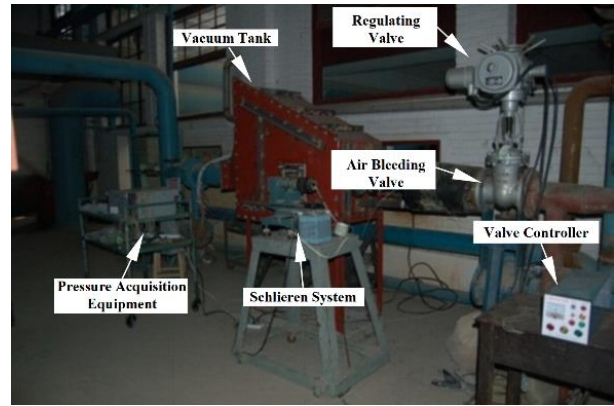
Computational Fluid Dynamics (CFD) serves as a crucial tool in investigating the dynamic flow characteristics of unsteady supersonic nozzles (Huang et al., 2022; Li et al., 2022; Rakhsha et al., 2023). Commercial simulation software, such as Fluent, has been widely used for SERN numerical calculations. To create a nozzle with optimal aerodynamic performance and seamless integration with the airframe, Yu et al. (2019) utilized the Method of Characteristics (MOC) for reverse design of the SERN. This reverse design methodology involves manipulating the nozzle exit to achieve the desired shape and flow parameters, followed by the application of the MOC technique to generate the nozzle contour in a reverse manner. The accuracy and validity of this method were verified using Fluent. Huang et al. (Huang et al., 2013) employed the Reynolds-Averaged Navier-Stokes (RANS) methodology, utilizing the Renormalization Group (RNG) k-ε turbulence model, for the purpose of resolving and examining the flow properties within SERN. They also utilized data mining techniques and combined them with experimental data to further investigate the flow characteristics. The research findings demonstrated that the employed model exhibited a favorable 2D structure, and the results were highly consistent with the experimental data. Yu et al. (2014a) employed Fluent to examine the separation characteristics in overexpanded SERNs and their impact on performance. SERNs display a prevailing separation pattern referred to as restricted shock separation (RSS), while free shock separation (FSS) can only be observed at specific nozzle pressure ratios (*NPR*). This behavior differs remarkably from that of axisymmetric rocket nozzles. The transition between these separation patterns has a notable impact on the performance of SERNs, especially in terms of lift. Mousavi et al. (Mousavi et al., 2018) utilized Fluent to investigate the effects of wall temperature discontinuity jump and changes in the length of the flap on the flow characteristics of overexpanded SERN. The findings indicate that modifications in flap length and wall temperature exert a notable influence on the interplay between shock waves and boundary layers, as well as on the structure, intensity, and spacing of λ shock waves.

Free open-source software, such as OpenFOAM, offers advantages in terms of security, quality, flexibility and affordability compared with commercial simulation software. OpenFOAM, a popular open-source CFD tool, uses C++ as its programming language. Currently, OpenFOAM is primarily applied in the field of subsonic incompressible flows. Several scholarly reports have documented the utilization of OpenFOAM for researching subsonic compressible flows, including examinations of the wake generated by a circular cylinder (Bhattacharya & Ahmed, 2010; Joshi & Bhattacharya, 2019; Bhattacharya & Gregory, 2020) and the flow characteristics over a hemispherical turret mounted on a wall (Bhattacharya & Ahmed, 2020; Jia et al., 2021). However, research on compressible flows at supersonic speeds using OpenFOAM is relatively limited (Nair et al., 2022). Furthermore, most studies using OpenFOAM for supersonic nozzles have focused on under-expanded conditions, with limited research on overexpanded nozzles. Zang et al. (Zang et al., 2017) numerically studied an under-expanded supersonic nozzle at a Mach number of 1.45. The rhoCentralFoam solver in OpenFOAM was employed to conduct a flow simulation, and compared the results with Fluent. The velocity distribution at the jet outlet and the downstream structure formed exhibited noteworthy concurrence in both 2D and 3D unsteady RANS results, indicating a robust consistency between the two solvers. In addition, comprehensive 3D simulations using both solvers can generate reasonably realistic flow fields under the stated flow circumstances, as evidenced by qualitative and quantitative comparisons with other experimental results. Liu et al. (Liu et al., 2022) conducted 3D numerical simulations of nozzle thrust using the OpenFOAM. The findings indicate that the average plume flow can be regarded as an axisymmetric underexpanded supersonic jet.

The control equations for compressible flow problems are typically solved using methods based on pressure or density, both of which are widely employed in CFD (Shyji et al., 2017; John & Vivekkumar, 2020; Salimi et al., 2022). The pressure field in the pressure-based approach is determined by solving either the pressure equation or a pressure correction equation. The density-based approach solves for density in the continuity equation and calculates the pressure using the state equation. When dealing with compressible flow problems, density-based methods have certain advantages. These methods directly employ the density variable in the solution process and consider the influence of density variations on the flow while solving the governing equations. Consequently, they are particularly suitable for situations involving high-speed flows and large pressure gradients, where significant density variations occur. Density-based methods offer greater accuracy in capturing complex phenomena, such as shock waves and boundary
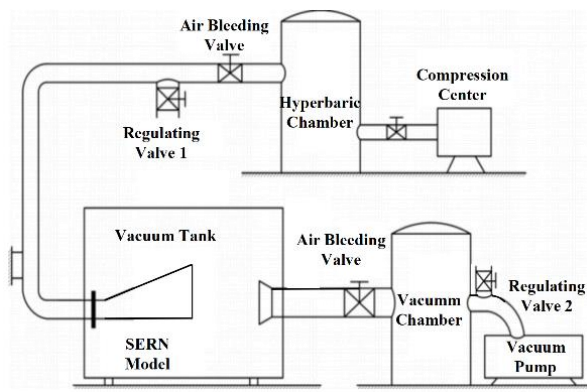
(a) Experimental wind tunnel structure schematic   (b) Experimental wind tunnel photo

Fig. 1 Experimental wind tunnel and related test equipment

layer separation. In OpenFOAM, both approaches are implemented as solvers: the pressure-based approach is represented by the sonicFoam solver, and the density-based approach is represented by the rhoCentralFoam solver. The rhoCentralFoam solver, based on the central upwind scheme is used for density compressible flow simulations (Kurganov et al., 2000; Kurganov & Tadmor, 2000).

In this study, the separation pattern and the transition of separation patterns in an overexpanded SERN were investigated using a combination of experimental and numerical simulations. A comparison between the two OpenFOAM solvers, rhoCentralFOAM and sonicFOAM, was performed to solve the flow field of the SERN. This provides a reference for experimental methods, boundary conditions, discretisation methods and solver selection for compressible flows in complex flow settings.

2. EXPERIMENTAL AND NUMERICAL METHODS
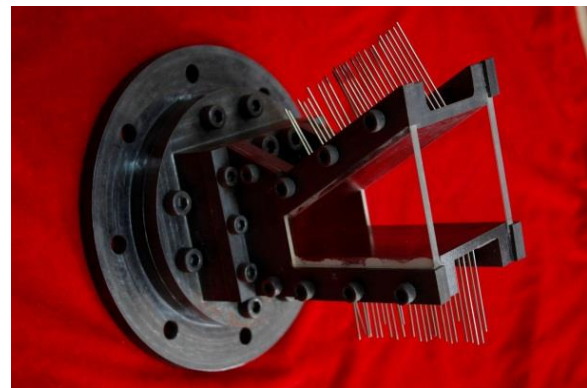
2.1 Experimental Setup and Models

The experimental setup for the wind tunnel has been previously described (Yu et al., 2015). The wind tunnel utilises an air source with both high and low-pressure capabilities. The air compressor supplies a high-pressure source ranging from 0.8 MPa to 0.9 MPa, and the vacuum pump provides a low-pressure environment of 3–5 kPa. The maximum achievable flow rate is 0.8 kg/s. The experimental equipment for the wind tunnel includes high

speed camera, schlieren system and pressure acquisition equipment. The schlieren system features a 'Z-shaped' configuration with a mirror diameter of 200 mm. A Canon 500D camera is used for schlieren photos and image recording, with a maximum resolution of 4752×3168 and a pixel size of approximately 22 μm^2. The camera's film shooting resolution is 1920×1080 at 20 frames per second. The IDT MotionPro Y5 high-speed camera has a maximum resolution of 2336×1728 and can shoot up to 730 frames per second. The camera's maximum shooting speed is 69,000 frames per second, corresponding to a resolution of 2336×16. The pressure acquisition system has an error of 0.05% of the full scale. The wind tunnel and related test equipment are shown in Fig. 1.

In the experiment, a 2D SERN with a 25° expansion angle and a corresponding flap was employed. The throat area of the nozzle (A_t) was 1200 mm^2, the expansion area ratio (A_e/A_t) was 2.896, and the width measured 60 mm. To enable convenient observation and documentation of the flow state and characteristics inside the nozzle, the side walls of the nozzle were fabricated using optical glass. The front of the nozzle features a 30 mm long circular-to-rectangular transition section. The circular diameter in the transition section is 66 mm, and the rectangular portion measures 60 mm in length and 38.5 mm in width. The inner profile of the transition section is obtained using the ruled surface method. The nozzle geometry details are depicted in Fig. 2(a), while a photograph of the experimental nozzle is presented in Fig. 2(b).
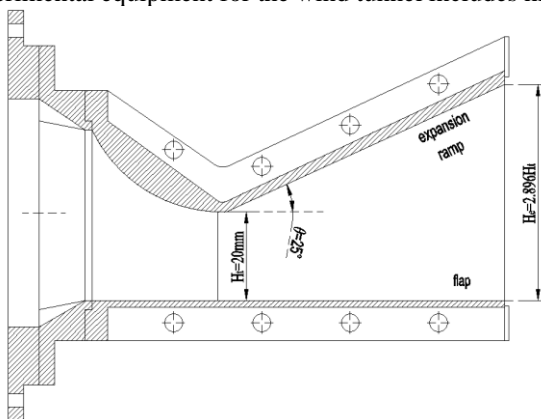
(a) Experimental nozzle geometry configuration   (b) Photograph of experimental nozzle

Fig. 2 SERN experimental model

Table 1 Pressure, velocity and temperature boundary conditions

	Pressure (P)	Velocity (U)	Temperature (T)
Inlet	totalPressure	zeroGradient	totalTemperature
Wall	zeroGradient	noSlip	zeroGradient
Far Field	waveTransmissive	waveTransmissive	waveTransmissive
Outlet	waveTransmissive	waveTransmissive	waveTransmissive

Table 2 Boundary conditions and parameters in Fluent

Property	Setting
Materials	Ideal-gas; compressible
Dimensionality	2D
Solver	Density-Based
Solve Method	Implicit
Turbulence Model	k-epsilon RNG
Near-Wall Treatment	Standard wall functions
Pressure Inlet	Total Pressure = 93243.66 Pa; Temperature = 300 K
Pressure Far Field	Ma=0; Pressure = 31073.02 Pa; Temperature = 300 K
Pressure Outlet	Pressure = 31073.02 Pa; Temperature = 300 K
Wall	Adiabatic
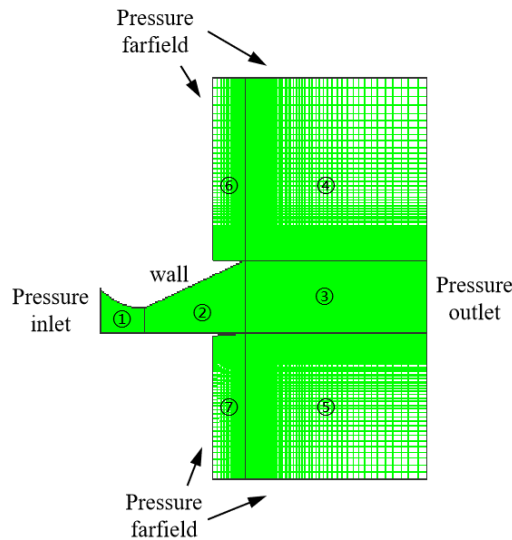
Fig. 3 Grid and boundary conditions of numerical simulation

2.2 Numerical Method

2.2.1 Boundary Conditions and Grids

The boundary conditions are consistent with the experimental conditions, with a *NPR* of 3.0. The total pressure at the inlet is 93243.66 Pa, and the temperature is 300 K. The Mach number at the far field is 0, with a pressure of 31073.02 Pa and a temperature of 300 K. The outlet is set with the same pressure and temperature values. The wall boundary is assigned with no-slip. Table 1 shows the details of the boundary condition settings in OpenFOAM, and Table 2 provides the boundary condition parameters in Fluent.

ICEM is used to structurally mesh the geometry of a straight-wall SERN. The grid and boundary conditions are named as illustrated in Fig. 3. The grid nodes for regions 1, 2, and 3 are 80×120, 180×120, and 100×120 in the *x* and *y* axes, respectively. Regions 4 and 5 have a grid size of 100×100, and regions 6 and 7 are set to 40×100.

2.2.2 Governing Equations

The 2D RANS equation is used to solve the flow (Yaravintelimath et al., 2016; Pathan et al., 2019; Gayathri et al., 2022). The governing equations are expressed as follows:
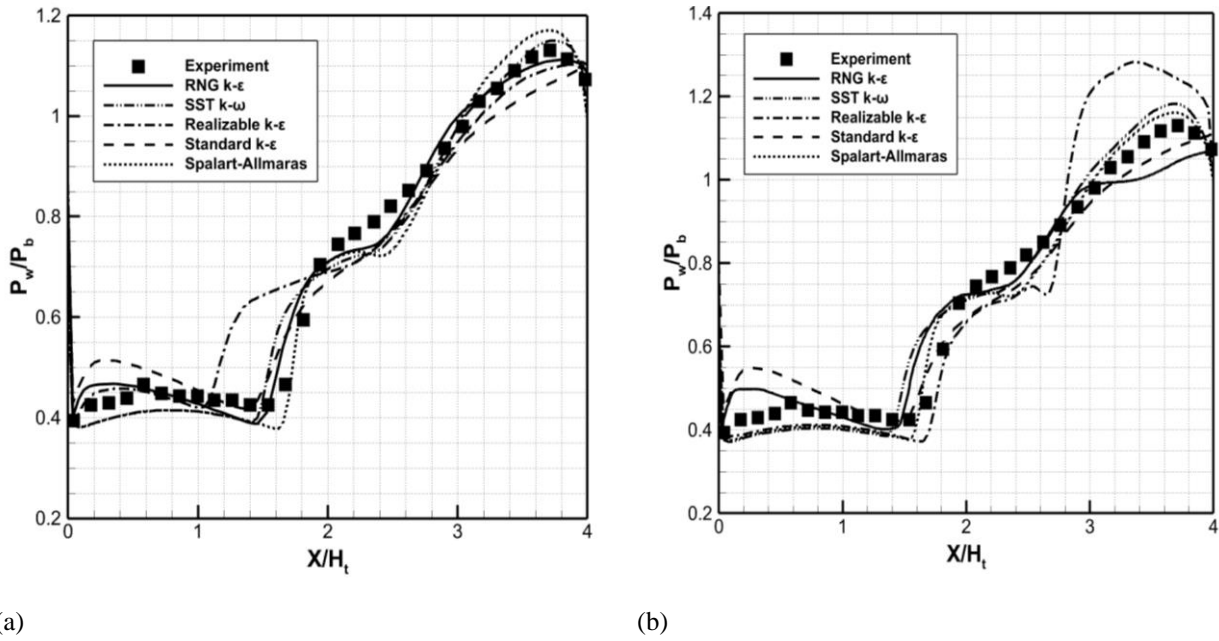
Mass conservation equation

$$\frac{\partial \rho}{\partial t} + \frac{\partial(\rho u_i)}{\partial x_i} = 0 \tag{1}$$

Momentum conservation equation

$$\frac{\partial(\rho u_i)}{\partial t} + \frac{\partial(\rho u_j u_i)}{\partial x_j} = -\frac{\partial \rho}{\partial x_i} + \frac{\partial \tau_{ij}}{\partial x_j} \tag{2}$$

Energy conservation equation

$$\rho \frac{D}{Dt}\left(e + \frac{V^2}{2}\right) = \rho \dot{q} + \frac{\partial}{\partial x_i}\left(k_{eff}\frac{\partial T}{\partial x_i}\right) - \frac{\partial(u_i p)}{\partial x_i} + \frac{\partial u_i \tau_{ij}}{\partial x_j} \tag{3}$$

(a)　　　　　　　　　　　　　　　　　　　　　　　(b)

Fig. 4 Pressure distribution on the expansion ramp under different turbulence models is compared with the experimental results of *NPR* = 3: (a) rhoCentralFOAM; (b) sonicFOAM

where, ρ represents density, u_i denotes velocity components, p stands for pressure, τ_{ij} represents the stress tensor, k_{eff} represents effective thermal conductivity, and $\dot{q}$ represents volumetric heat addition per unit mass.

2.2.3 Discretisation

SonicFOAM and rhoCentralFOAM both employ the Eulerian discretization scheme for the time term. These two solvers utilize the Gauss linear format for gradient calculations, while the discretization of the Laplacian term is done using the modified Gauss linear format. The former uses a linear scheme for the interpolation scheme, and the latter employs vanLeer interpolation for the reconstruction of T, U and rho. The turbulence terms for both solvers are discretised using the upwind format, and the surface normal gradient scheme utilizes the corrected scheme. The remaining terms in the sonicFOAM divergence scheme utilize a second-order scheme called Gauss limitedLinear 1. This scheme effectively limits upwind in zones with rapidly changing gradients. The '1' indicates a strong limit. The divergence scheme of rhoCentralFOAM is Gauss linear.

2.2.4 Solution and Control Schemes

In sonicFOAM, the diagonal solver is utilized for solving rho, while the smoothSolver incorporates symGaussSeidel to handle other discretisation terms. The rhoCentralFOAM solver utilizes the diagonal solver to solve for the variable rho, while the turbulence term is addressed through the smoothSolver and Gauss-Seidel solver. The remaining terms are solved using the Geometric agglomerated Algebraic MultiGrid solver and Gauss-Seidel smoother. The time step is set at 1e−8 s with adaptive control, and the simulation concludes at 0.02 s, generating solution outputs every 1e−4 s.

3.　RESULTS AND DISCUSSION

### 3.1 Comparative Study of Different Turbulence Models

Numerical calculations were performed on an over-expanded SERN using various turbulence models in the rhoCentralFOAM and sonicFOAM solvers. The obtained results were compared with experimental data, as shown in Fig. 4, where the *x* and *y* parameters are non-dimensional. X/H$_t$ represents the ratio of nozzle length to throat height, and P$_w$/P$_b$ represents the ratio of wall pressure to ambient pressure. In the results of rhoCentralFOAM, the predicted deviations at the separation point for different turbulence models are as follows: RNG *k-ε* model is 0.0806, SST *k-ω* model is 0.1123, realizable *k-ε* model is 0.4962, standard *k-ε* model is 0.1581, and Spalart-Allmaras model is 0.0814, as shown in Fig. 4(a). Meanwhile, in the results obtained from sonicFOAM, the corresponding deviations are as follows: RNG *k-ε* model is 0.0914, SST *k-ω* model is 0.1744, realizable *k-ε* model is 0.1141, standard *k-ε* model is 0.0361, and Spalart-Allmaras model is 0.0272, as shown in Fig. 4(b). Additionally, Fig. 4 reveals specific trends in the predicted pressure distributions. Both the SST *k-ω* and Spalart-Allmaras models underestimate the pressure ahead of the separation shock in rhoCentralFOAM and sonicFOAM. The standard *k-ε* model significantly overestimates the pressure in that region. Notably, in sonicFOAM, the realizable *k-ε* model severely overestimates the pressure at the nozzle trailing edge. Based on these observations, it can be concluded that the RNG *k-ε* model accurately predicts the flow separation location in the over-expanded SERN. Therefore, for further investigation, the RNG *k-ε* model is selected as the preferred turbulence model.
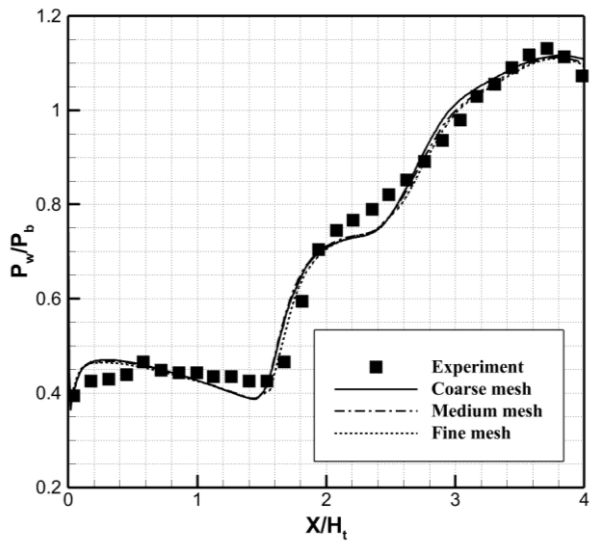
Fig. 5 RhoCentralFOAM solves three different resolution grids, and the computational results are compared with experiments to evaluate the accuracy of the simulations
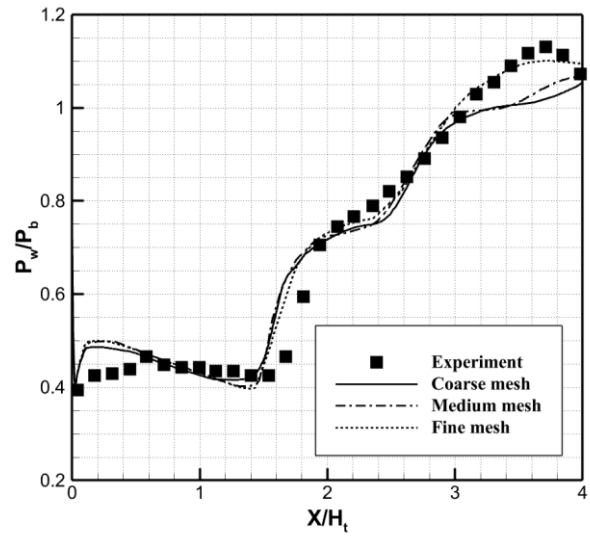
Fig. 6 SonicFOAM solves three different resolution grids, and the computational results are compared with experiments to evaluate the accuracy of the simulations
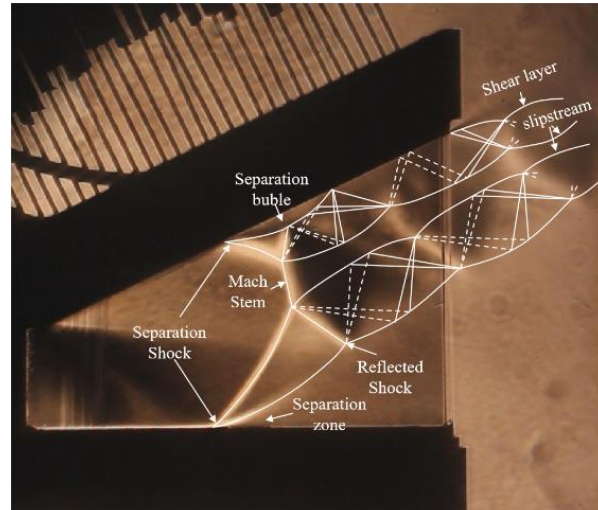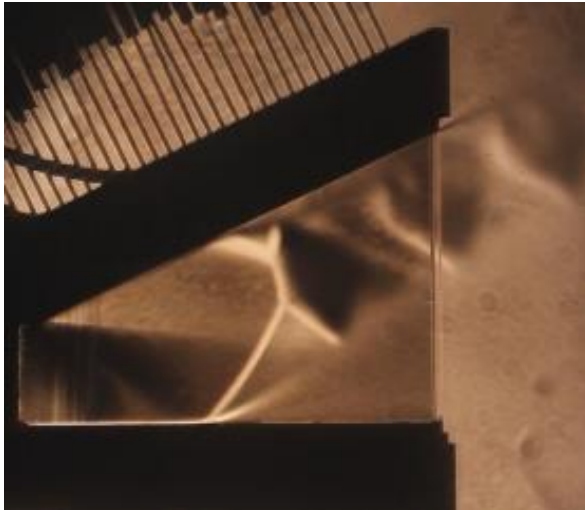

Fig. 7 Experimental schlieren flow field of the SERN at *NPR* of 3, demonstrating the RSS (ramp) pattern separation: (a) experimental flow field visualisation; (b) labelled main shock wave structure

The grid independence of the rhoCentralFOAM and sonicFOAM solvers is verified to validate their accuracy. Three different grid scales are used: the medium grid (69,807 cells) described above, the fine grid (282,007 cells) with twice as many grid nodes in both *x* and *y* directions; and the coarse grid (17,107 cells) with half as many grid nodes in both *x* and *y* directions. Fig. 5 shows the pressure distribution on the expansion ramp calculated by the rhoCentralFOAM for each grid. With the change in grid sparsity, the expansion ramp separation point location remains nearly identical, and the pressure distribution is comparable, with a divergence of less than 3%, which is within the acceptable range. The medium grid can be utilised to achieve acceptable calculation precision. Fig. 6 shows the pressure distribution along the expansion ramp obtained through calculations performed by the sonicFOAM solver for each grid. With the change in grid sparsity, the separation point on the expansion ramp shifts slightly, and the pressure distribution undergoes

remarkable shifts compared with rhoCentralFOAM. However, the overall change is within an acceptable range, and satisfactory calculation accuracy can be obtained by using a medium grid for the relevant calculations. In addition, the accuracy of Fluent has been confirmed in the literature (Yu, 2020).

3.2 Study on Flow Separation Pattern of Overexpanded SERN

Figure 7 shows the Mach stem formation that occurs when separated shock waves from the ramp and the flap intersect and reflect, along with the characteristic Mach reflection (MR) structure known as the "λ" shock wave pattern. After the flow separates at the expansion ramp of the SERN, it reattaches downstream, forming a closed separation bubble typical of the RSS (ramp) pattern separation flow field. In addition, when the separation shock wave of an ramp interacts with a Mach stem, a reflected shock wave is formed. It interacts with the
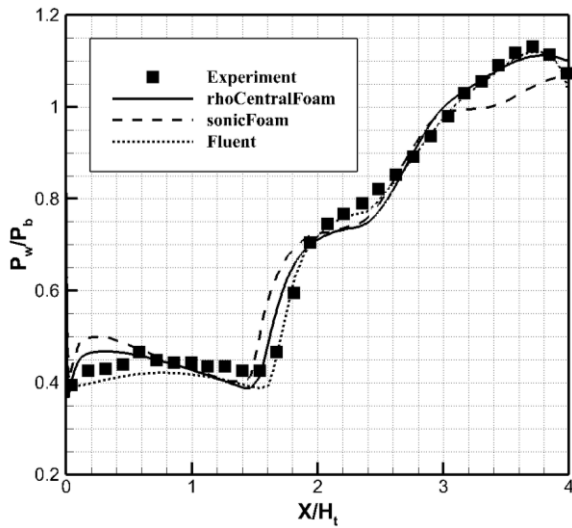
Fig. 8 Comparison of the expansion ramp pressure distribution calculated by rhoCentralFOAM, sonicFOAM and Fluent with experimental results at an *NPR* of 3

Fig. 9 Comparison of the flap pressure distribution calculated by rhoCentralFOAM, sonicFOAM and Fluent with experimental results at an *NPR* of 3

boundary of the separation bubble and reflects, thus forming an expansion wave. The expansion wave interacts with the subsonic flow boundary formed behind the Mach stem, reflecting again to form a compression wave, gradually propagating along the ramp and slip line. Compared to the separation shock wave and reflected shock wave formed by the ramp, the flow on the flap does not reattach. Therefore, the separation shock wave on the flap and the subsequent reflected shock wave interact with the aerodynamic boundary of the flow and are not influenced by the nozzle wall.

Figure 8 presents a comparison of the pressure distribution on the expansion ramp calculated by rhoCentralFOAM, sonicFOAM and Fluent at *NPR* of 3, along with the experimental results. The wall pressure distributions obtained from rhoCentralFOAM, sonicFOAM, and Fluent exhibit satisfactory agreement with the experimental data. Nevertheless, variations are observed in the handling of intricate flow field aspects. Both rhoCentralFOAM and sonicFOAM overestimate the pressure of the expansion wave fan at the nozzle throat, with sonicFOAM exhibiting a greater overestimation. Fluent outperforms rhoCentralFOAM and sonicFOAM in accurately capturing the location of the expansion ramp separation point, as rhoCentralFOAM and sonicFOAM predict the separation point location approximately 0.077 and 0.1 units in advance, respectively. The pressure at the separation point of the expansion ramp is comparable amongst rhoCentralFOAM, sonicFOAM and Fluent, but slightly lower than the experimental data. The platform pressure after the separation shock wave is lower for rhoCentralFOAM and sonicFOAM, whereas Fluent closely matches the experimental values, indicating that rhoCentralFOAM and sonicFOAM underestimate the intensity of the separation shock wave at the expansion ramp. Moreover, rhoCentralFOAM, sonicFOAM and Fluent accurately capture the reattachment location following the separation bubble. The expansion ramp pressure distribution increases rapidly after the separation bubble in rhoCentralFOAM and Fluent, whereas the
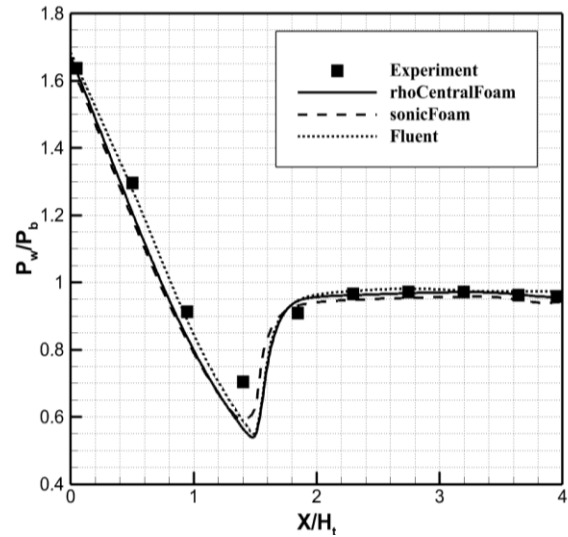
pressure increase trend in sonicFOAM is relatively slow. The pressure drop observed in the sonicFOAM solver is due to presence of an expansion wave near the nozzle outlet resulting from to shock/shock or shock/slipstream interactions.

Figure 9 presents a comparison of the pressure distribution on the flap, obtained from rhoCentralFOAM, sonicFOAM, Fluent, and experimental results, for an *NPR* of 3. Prior to the separation point, the pressure distribution agrees reasonably well with the experimental data for Fluent, whereas it appears relatively lower for rhoCentralFOAM and sonicFOAM. After the separation shock wave, the pressure distributions in rhoCentralFOAM, sonicFOAM and Fluent align well with the experimental data.

Figure 10 shows the experimental schlieren and numerical schlieren images of rhoCentralFOAM, sonicFOAM and Fluent at *NPR*=3.0. The numerical schlieren represents the density gradient contour. The information in the flow field is modified because of the high-density gradient near the wall. In Fig. 10 (a), the separation pattern is RSS (ramp). The figure clearly shows the expansion fan at the throat and the MR formed by the separation shock wave. Figs. 10(b), 10(c) and 10(d) depict the numerical schlieren of rhoCentralFOAM, sonicFOAM and Fluent, respectively, showing that all three simulations capture the expansion wave fan at the throat, the separation bubble occurring on the ramp and its corresponding MR. The numerical schlieren of rhoCentralFOAM, sonicFOAM and Fluent shows that the flow field is dominated by the RSS pattern. The numerical simulation results obtained from rhoCentralFOAM, sonicFOAM, and Fluent all exhibit the presence of the RSS (ramp) pattern in the flow field, successfully capturing expansion waves, separation bubbles, and the MR phenomenon, as shown in Figs. 10(b), 10(c) and 10(d). A comparison between the numerical schlieren of rhoCentralFOAM, sonicFOAM and Fluent with the experimental schlieren reveals that Fluent exhibits the.
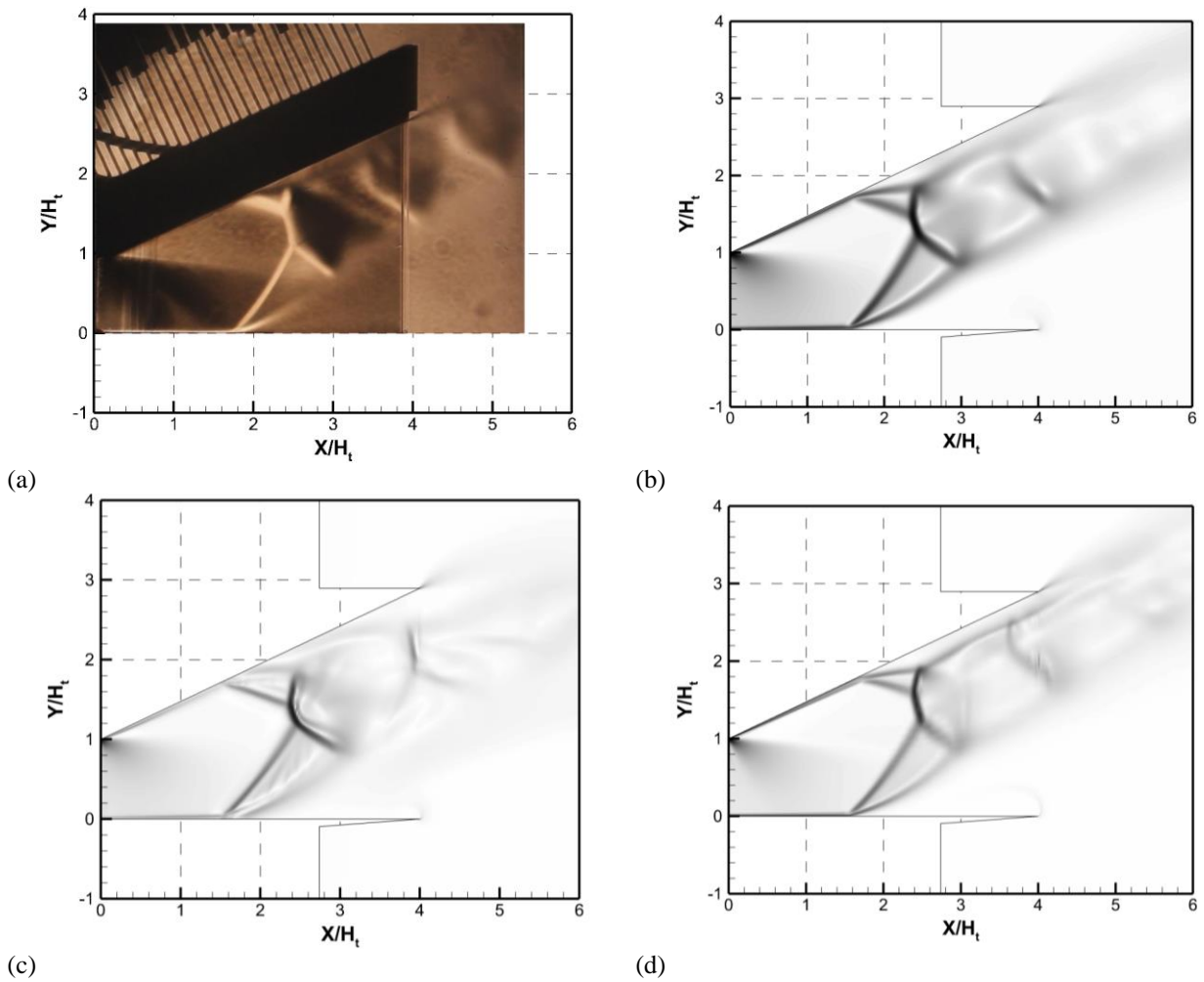
Fig. 10 Comparison of the flow fields calculated by rhoCentralFOAM, sonicFOAM, and Fluent with experimental results at an *NPR* of 3: (a) Experimental schlieren ; (b) rhoCentralFOAM numerical schlieren ; (c) sonicFOAM numerical schlieren ; (d) Fluent numerical schlieren
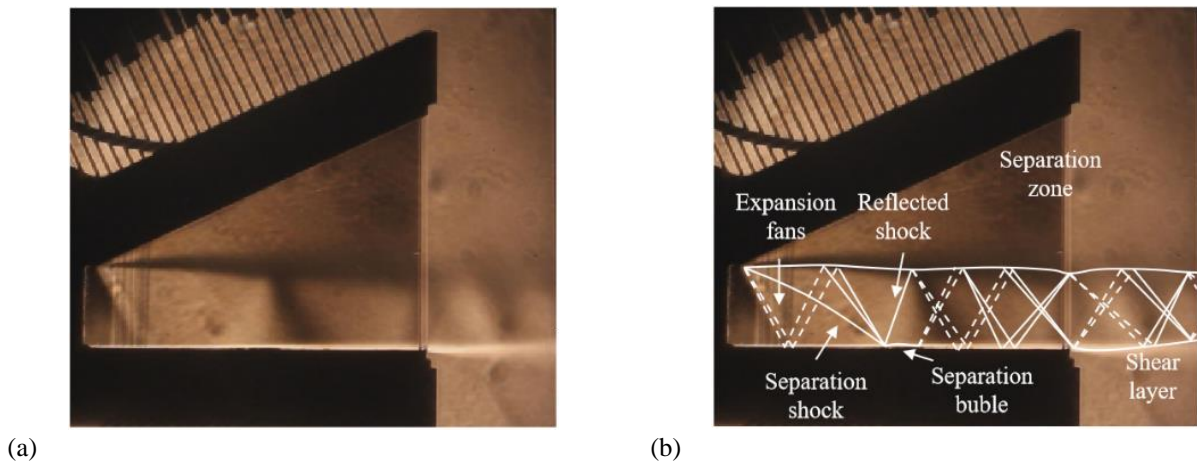
Fig. 11 Experimental flow field schlieren of SERN when *NPR* is 2.3, and the separation pattern is RSS (flap) pattern: (a) experimental flow field; (b) labelled main shock wave structure

highest degree of reduction in the SERN flow field structure, followed by rhoCentralFOAM. Both rhoCentralFOAM and sonicFOAM exhibit a tendency to overestimate the length of the separation shock wave on the expansion ramp and underestimate its intensity. Consequently, this gives rise to disparities in the MR formed by the separation shock wave. Specifically, the

Mach stem is positioned at a greater distance from the expansion ramp and has a reduced length, leading to discrepancies in the configuration of the 'λ' shock and the spacing between the 'λ' shocks

Figure 11 shows the RSS (flap) pattern experimental flow field schlieren at SERN. Figure 11(a) shows the flow

(a)

(b)

(c)

(d)

Fig. 12 Comparison of the flow fields calculated by rhoCentralFOAM, sonicFOAM, and Fluent with experimental results at an *NPR* of 2.3: (a) Experimental schlieren; (b) rhoCentralFOAM numerical schlieren; (c) sonicFOAM numerical schlieren; (d) Fluent numerical schlieren
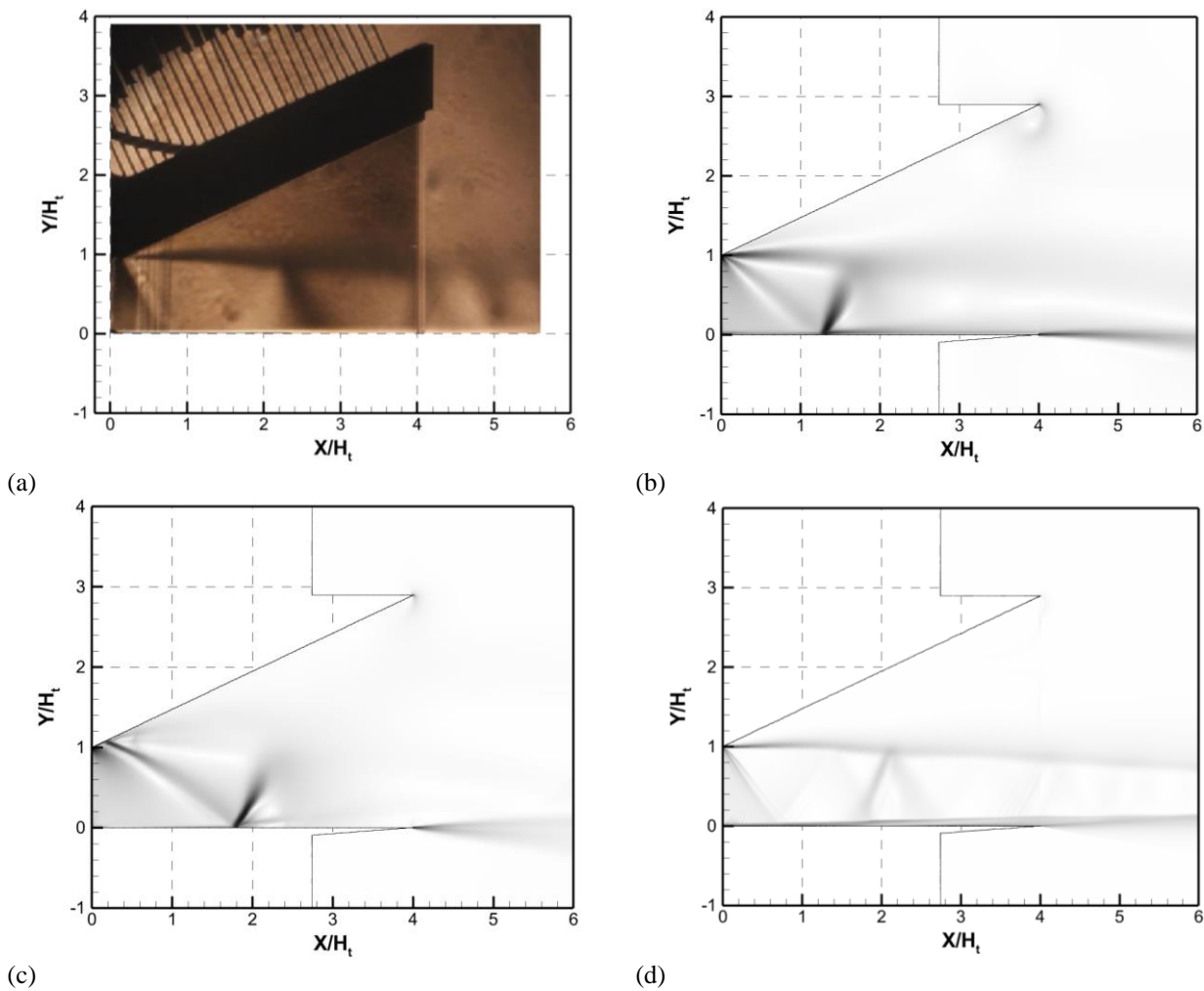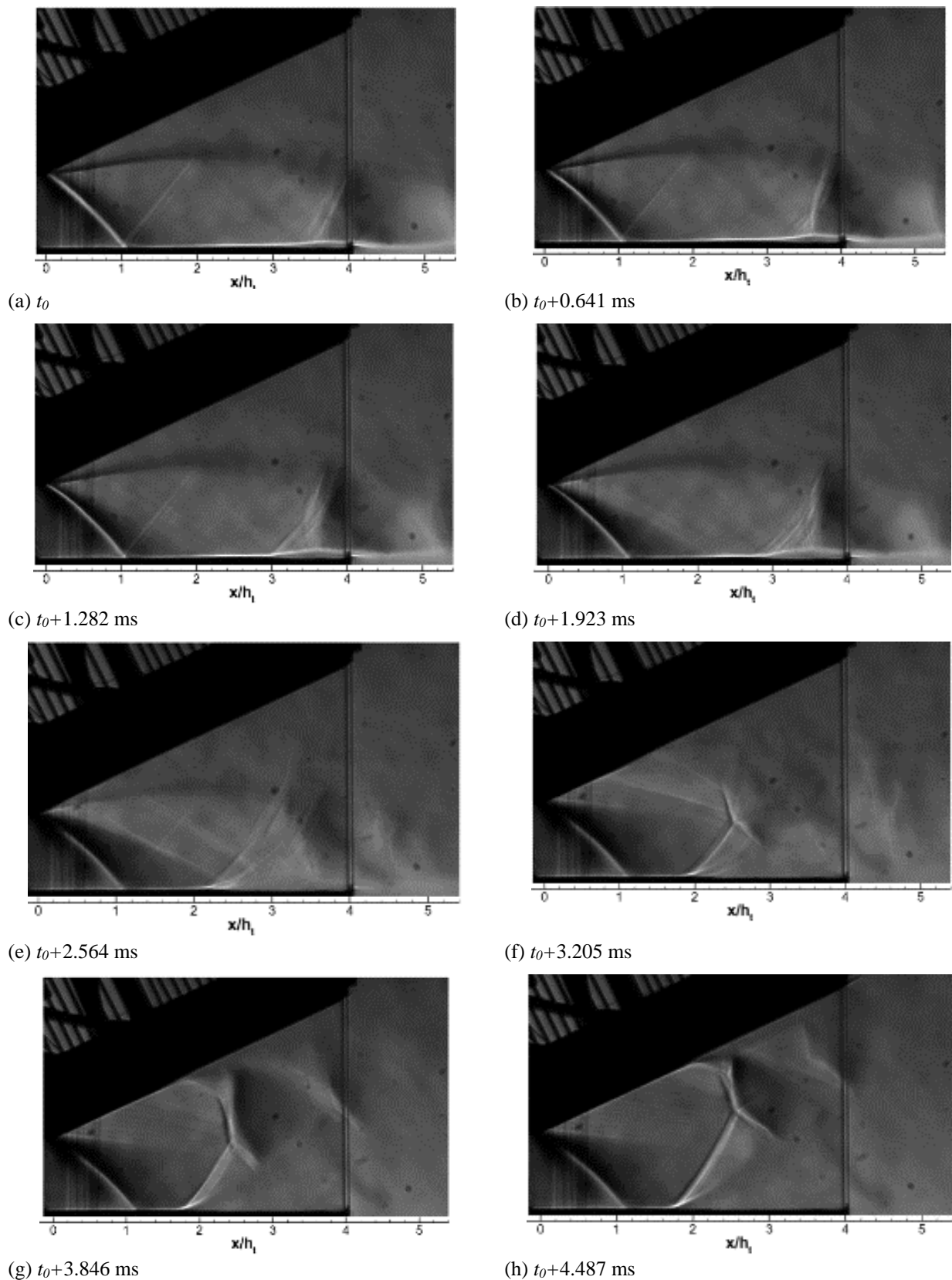
field image captured at an *NPR* of 2.3, while Fig.11(b) highlights the main shock wave structure. At this time, SERN is in a serious overexpansion state, and separation bubbles are forming on the flap. In the throat region, an expansion wave is generated, causing the flow direction to deflect upwards. When the expansion wave encounters the flap, it undergoes reflection and interacts with the aerodynamic boundary, resulting in a compression wave. The separation shock wave generated by the compression wave and the expansion ramp converges and reflects at the flap, creating a reflected shock wave, which leads to the formation of a separated bubble. The flow then reattaches to the flap, and the size of the separation bubble is extremely small.

Figure 12 shows the experimental schlieren and numerical schlieren of rhoCentralFOAM, sonicFOAM and Fluent at *NPR*=2.3. The figures clearly demonstrate that both the experimental and numerical results exhibit a flow field structure dominated by the RSS (flap) pattern. At the throat of SERN, an expansion wave fan is generated, which is then reflected by the flap and interacts with the upper boundary layer, resulting in the formation of a compression wave. Separation shock waves generated at the ramp near the throat converge with the compression waves at the flap, leading to the generation of reflected

shock waves and separation bubbles, ultimately forming an RSS (flap) pattern. A comparison between the numerical simulation results of rhoCentralFOAM and sonicFOAM reveals that sonicFOAM produces a longer separation shock wave and has a more aft separation point location on the ramp.

3.3 Study on Flow Separation pattern Transition of Overexpanded SERN

Previous studies (Nave & Coffey, 1973) investigated separation patterns and transitions in rocket nozzles, which also exist in SERNs. However, the forces resulting from these transitions, known as lateral loads in rocket nozzles, act in the lift direction in SERN. Therefore, the transition of separation pattern poses a considerable challenge, affecting both its structural strength and control system, given the sudden changes in performance. During the transition of the separation pattern in the rocket nozzle, a large Mach number disc is formed, which affects only a limited region of the jet situated behind and in proximity to the separation shock wave boundary. In the case of SERN, the occurrence of normal shock waves is absent or extremely rare when operating in both FSS and RSS patterns. Consequently, notable modifications take place in the flow field during the separation pattern transition,

(a) t_0

(b) $t_0+0.641$ ms

(c) $t_0+1.282$ ms

(d) $t_0+1.923$ ms

(e) $t_0+2.564$ ms

(f) $t_0+3.205$ ms

(g) $t_0+3.846$ ms

(h) $t_0+4.487$ ms

Fig. 13 Transition process from RSS (flap) to RSS (ramp) captured by high-speed camera during the experiment: (a) t_0; (b) $t_0+0.641$ ms; (c) $t_0+1.282$ ms; (d) $t_0+1.923$ ms; (e) $t_0+2.564$ ms; (f) $t_0+3.205$ ms; (g) $t_0+3.846$ ms; (h) $t_0+4.487$ ms

leading to a shift in the direction of the SERN jet. These modifications exert a substantial influence on the performance of the SERN.

Our team conducted experimental filming of the transition process of SERN, as depicted in Fig. 13 (Yu et al., 2015). Initially, the separation shock wave of the flap

became unstable and gradually moved towards the throat, resulting in an enlargement of the separation bubble. Subsequently, as the separation shock wave reached a critical position, the separation bubble opened, allowing ambient flow to enter and form a recirculation region. Under the influence of the separation shock wave, the flow diverted upwards. At this stage, the flow began to expand on the expansion ramp, leading to the formation of a new separation shock wave. The intersection and reflection of the two separation shock waves created two asymmetric "λ" waves. Afterwards, the flow field structure gradually stabilized, completing the transition within a duration of no more than 5 ms

Numerical simulation plays a pivotal role in the investigation of the flow separation pattern transition process. The inherent rapidity of the transition poses difficulties in directly observing and documenting the flow field characteristics. Through the utilization of numerical simulation, we can effectively analyze the subtle alterations occurring within the flow field throughout the transition. In this section, the separation pattern transition of SERN was studied using the rhoCentralFOAM and sonicFOAM solvers to assess their predictive performance for the separation pattern transition of an overexpanded SERN. The codedFixedValue boundary condition was used to increment the *NPR* of the model by 0.2 per 0.01 s, with a

time step is 1e−8 s. Although the *NPR* changes rapidly, previous research (Yu et al., 2014a) demonstrated that the separation transition is not solely caused by the rapid *NPR* variation but rather by an inherent instability phenomenon. The numerical simulation results in the later section indicate that the chosen *NPR* change rate yields a more accurate separation pattern transition outcome.

Figure 14 shows the Mach contours during the transition from RSS (flap) to FSS and then to RSS (ramp) in separation pattern transition, as obtained from the rhoCentralFOAM numerical simulation. The simulation captures the changes in the SERN flow field during the transition, aligning with the experimental results. As the *NPR* of SERN is progressively increased, the transition process from the RSS (flap) pattern to the FSS pattern begins to occur. During this process, the main jet of the nozzle gradually deflects upward, and the separated bubble on the flap opens, allowing ambient air to enter the recirculation region. According to the numerical simulation results in Fig. 14, it is observed that the *NPR* at the start of this transition process is 2.4771, and it reaches 2.4790 at the end. After the completion of this phase, the shift from the FSS (flap) configuration to the RSS (ramp) configuration commences. During this stage, the primary jet of the nozzle reconnects with the expansion ramp, leading to a rapid downstream movement of the separation point. The alteration in the trajectory of the main jet within

(a) t_0, *NPR*=2.4771

(b) t_0+0.1 ms, *NPR*=2.4790

(c) t_0+1.9 ms, *NPR*=2.5137
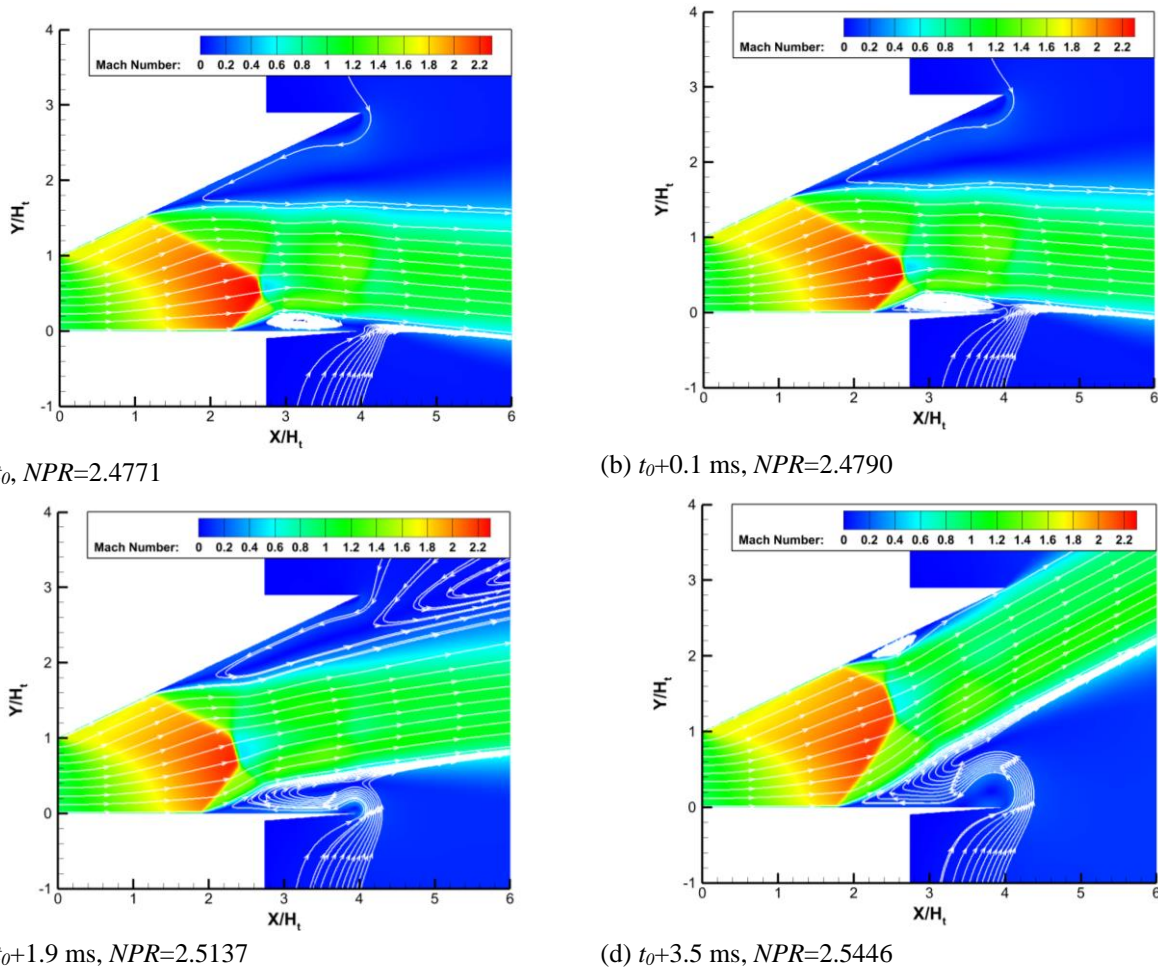
(d) t_0+3.5 ms, *NPR*=2.5446

Fig. 14 Separation pattern transition from RSS (flap) to FSS to RSS (ramp) in rhoCentralFOAM simulation: (a) t_0, *NPR*=2.4771; (b) t_0+0.1 ms, *NPR*=2.4790; (c) t_0+1.9 ms, *NPR*=2.5137; (d) t_0+3.5 ms, *NPR*=2.5446

(a) t_0, *NPR*=2.3998

(b) t_0+0.1 ms, *NPR*=2.4017

(c) t_0+1.9 ms, *NPR*=2.4365
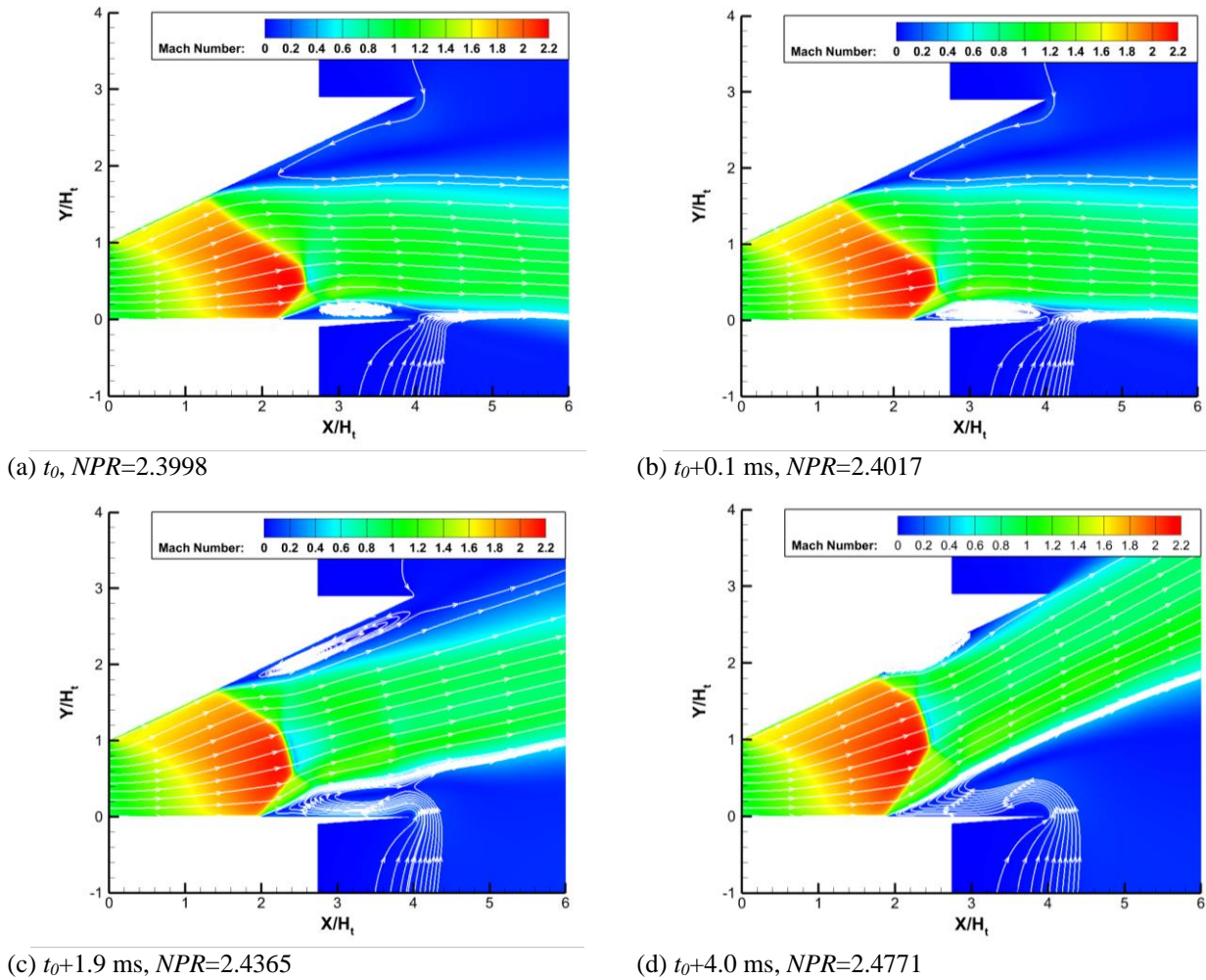
(d) t_0+4.0 ms, *NPR*=2.4771

Fig. 15 Separation pattern transition from RSS (flap) to FSS to RSS (ramp) in sonicFOAM simulation: (a) t_0, *NPR*=2.3998; (b) t_0+0.1 ms, *NPR*=2.4017; (c) t_0+1.9 ms, *NPR*=2.4365; (d) t_0+4.0 ms, *NPR*=2.4771

the nozzle can significantly impact the performance of the SERN in the over-expanded state. Based on the outcomes of numerical simulations, the *NPR* at the initiation of this transition process is recorded as 2.4790, progressively reaching 2.5446 at the conclusion. The entire duration of the transition process, encompassing the shift from the RSS (flap) pattern to the RSS (ramp) pattern, spans approximately 3.5 ms, accompanied by a *NPR* variation of 0.0675.

Figure 15 shows the Mach contours captured during the transition of the separation pattern from the RSS (flap) pattern to the FSS pattern and subsequently to the RSS (ramp) pattern, as simulated using the sonicFOAM numerical method. Similarly, the transition process from the RSS (flap) pattern to the FSS pattern initiates with a gradual increase in the *NPR* at SERN. The results obtained from the numerical simulation depicted in Fig. 15 reveal that the transition of the separation pattern commences at an *NPR* value of 2.3998 and concludes at an *NPR* value of 2.4017. Subsequently, the transition from the FSS pattern to the RSS (ramp) pattern takes place, commencing at an *NPR* of 2.4017 and concluding at an *NPR* of 2.4771. The entire transition process, encompassing the shift from the RSS (flap) pattern to the RSS (ramp) pattern, spans approximately 4.0 ms, with an *NPR* variation of 0.0773. Compared with rhoCentralFOAM, the sonicFOAM

transition process lasts longer and exhibits a greater *NPR* variation.

4. CONCLUSION

In this study, experimental studies and numerical simulations were conducted on over-expanded SERN. The separation patterns and transformation of the over-expanded SERN were compared between numerical calculations and experimental results. The predictive performance of two compressible flow solvers, rhoCentralFOAM and sonicFOAM, in OpenFOAM, was evaluated for over-expanded SERN, and their ability to predict complex flow states are evaluated.

Both rhoCentralFOAM and sonicFOAM accurately matched the experimental data for wall pressure distributions. However, both solvers predicted the location of the expansion ramp separation point slightly in advance, with rhoCentralFOAM being approximately 0.077 off and sonicFOAM being approximately being 0.1 off. Both the rhoCentralFOAM and sonicFOAM solvers exhibit relatively accurate numerical simulations for the flow separation problem in an overexpanded SERN. They successfully capture the characteristic RSS (ramp) pattern and the RSS (flap) pattern. Regarding the RSS (ramp) pattern, both solvers effectively predict the shock structure

across the entire flow field, encompassing the expansion wave at the throat, the separation bubble at the expansion ramp, and the 'λ' shock waves within the flow field. However, both models tend to overestimate the length and intensity of the separation shock wave occurring on the expansion ramp. The configuration of the 'λ' shock wave deviates from the experimental structure, and the spacing between 'λ' shock waves is shorter in sonicFOAM. In the RSS (flap) pattern, the separation point in the sonicFOAM results is further downstream, thereby exaggerating the length of the separation shock wave.

Both rhoCentralFOAM and sonicFOAM solvers accurately predicted the separation pattern transition process for the overexpanded SERN. However, differences are observed in the starting and ending *NPR*s of the RSS (flap) pattern to FSS pattern to RSS (ramp) pattern transition. SonicFOAM predicted the transition to start 0.0773 *NPR* earlier and end 0.0675 *NPR* earlier than rhoCentralFOAM. In addition, the sonicFOAM transition process takes slightly longer and the *NPR* variation is greater.

SonicFOAM cannot be recommended as a solver for the separation pattern of an overexpansion nozzle because it can not accurately predict the pressure rise after the separation bubble, reattachment shock wave, and exhibited an overestimation of the separation shock length. In future research, more accurate turbulence models that can better simulate turbulence behaviour and separation phenomena in compressible fluids should be considered. One potential approach to explore is the utilisation of large eddy simulation (LES) or a hybrid model that combines RANS with LES. Additionally, enhancing or developing new solvers for OpenFOAM are possible to improve numerical stability, computational efficiency, and convergence.

ACKNOWLEDGEMENTS

CONFLICT OF INTEREST

The authors declared that they have no conflicts of interest to this work.

We declare that we do not have any commercial or associative interest that represents a conflict of interest in connection with the work submitted.

AUTHORS CONTRIBUTION

T. Yu: Conceptualization; Data collection; Visualization; Writing the original draft. Y. Yu: Conceptualization (supporting); writing; review and editing. Y. P. Mao: Writing original draft (Supporting), review and editing. Y. L. Yang: Supervision, review and editing. S. L. Xu: Supervision, review and editing.

REFERENCES

Bhattacharya, S., & Ahmed, A. (2010). *Effect of sinusoidal forcing on the wake of a circular cylinder.* 48th AIAA Aerospace Sciences Meeting Including the New Horizons Forum and Aerospace Exposition. American Institute of Aeronautics and Astronautics. https://doi.org/10.2514/6.2010-89

Bhattacharya, S., & Ahmed, A. (2020). Effect of aspect ratio on the flow over a wall-mounted hemispherical turret. *International Journal of Heat and Fluid Flow*, 84, 108600. https://doi.org/10.1016/j.ijheatfluidflow.2020.108600

Bhattacharya, S., & Gregory, J. W. (2020). The effect of spatially and temporally modulated plasma actuation on cylinder wake. *AIAA Journal*, 58(9), 3808–3818. https://doi.org/10.2514/1.J059269

Edwards, C., Small, W., Weidner, J., & Johnston, P. (1975). *Studies of scramjet/airframe integration techniques for hypersonic aircraft*. 13th Aerospace Sciences Meeting (Vol. 1–0). American Institute of Aeronautics and Astronautics. https://doi.org/10.2514/6.1975-58

Gayathri, N., Senthilkumar, P., Dineshkumar, K., Purusothaman, M., & Sriharan, B. (2022). CFD analysis on flow through nozzle of conical type and truncated conical plug type. *Materials Today: Proceedings*. https://doi.org/10.1016/j.matpr.2022.09.407

Hemmati, A., & Namazian, Z. (2021). Numerical analysis of shock wave train in single-expansion ramp nozzle under harmonic inlet and outlet conditions. *Chemical Engineering Communications*, 1–10. Https://Doi.Org/10.1080/00986445.2021.2007091

Huang, S., Xu, J., Yu, K., Wang, Y., Pan, R., Chen, K., & Zhang, Y. (2022). Numerical study of a trapezoidal bypass dual throat nozzle. *Chinese Journal of Aeronautics*. https://doi.org/10.1016/j.cja.2022.11.015

Huang, W., Wang, Z., Ingham, D. B., Ma, L., & Pourkashanian, M. (2013). Design exploration for a single expansion ramp nozzle (SERN) using data mining. *Acta Astronautica*, 83, 10–17. https://doi.org/10.1016/j.actaastro.2012.09.016

Jia, K., Scofield, T., Wei, M., & Bhattacharya, S. (2021). Vorticity transfer in a leading-edge vortex due to controlled spanwise bending. *Physical Review Fluids*, 6(2), 024703. https://doi.org/10.1103/PhysRevFluids.6.024703

John, B., & Vivekkumar, P. (2020). A Numerical investigation on the equivalence of shock−wave/boundary-layer interactions using a two equations RANS model. *Journal of Applied Fluid Mechanics*, 14(3), 753–767. https://doi.org/10.47176/jafm.14.03.31722

Joshi, K., & Bhattacharya, S. (2019). Large-eddy simulation of the effect of distributed plasma forcing on the wake of a circular cylinder. *Computers & Fluids*, 193, 104295. https://doi.org/10.1016/j.compfluid.2019.104295

Kurganov, A., & Tadmor, E. (2000). New high-resolution central schemes for nonlinear conservation laws and convection–diffusion equations. *Journal of Computational Physics*, 160(1), 241–282. https://doi.org/10.1006/jcph.2000.6459

Kurganov, A., Guergana, A., & Siam, P. (2000). Semidiscrete central-upwind schemes for hyperbolic conservation laws and Hamilton—Jacobi equations. *SIAM Journal on Scientific Computing*, 23, 707–740. https://doi.org/10.1137/S1064827500373413

Lederer, R., & Krueger, W. (1993). *Nozzle development as a key element for hypersonics.* 5th International Aerospace Planes and Hypersonics Technologies Conference. American Institute of Aeronautics and Astronautics. https://doi.org/10.2514/6.1993-5058

Li, Z., Leng, J., Abu-Hamdeh, N. H., Abusorrah, A. M., & Musa, A. (2022). Effects of nozzle types on mass diffusion mechanism of hydrogen multi-jets at supersonic combustion chamber. *International Communications in Heat and Mass Transfer*, 139, 106509. https://doi.org/10.1016/j.icheatmasstransfer.2022.106509

Liu, X. Y., Cheng, M., Zhang, Y. Z., & Wang, J. P. (2022). Design and optimization of aerospike nozzle for rotating detonation engine. *Aerospace Science and Technology*, 120, 107300. https://doi.org/10.1016/j.ast.2021.107300

Mirjalily, S. A. A. (2023). Calibration of the k-ω shear stress transport turbulence model for shock wave boundary layer interaction in a SERN using machine learning. *Engineering Analysis with Boundary Elements*, 146, 96–104. https://doi.org/10.1016/j.enganabound.2022.10.009

Mousavi, S. M., Pourabidi, R., & Goshtasbi-Rad, E. (2018). Numerical investigation of over expanded flow behavior in a single expansion ramp nozzle. *Acta Astronautica*, 146, 273–281. https://doi.org/10.1016/j.actaastro.2018.03.003

Nair, P. P., Narayanan, V., Suryan, A., & Kim, H. D. (2022). Prediction and visualization of supersonic nozzle flows using OpenFOAM. *Journal of Visualization*, 25(6), 1227–1247. https://doi.org/10.1007/s12650-022-00856-5

Nave, L., & Coffey, G. (1973). *Sea level side loads in high-area-ratio rocket engines.* 9th Propulsion Conference. American Institute of Aeronautics and Astronautics. https://doi.org/10.2514/6.1973-1284

Pathan, K. A., Dabeer, P. S., & Khan, S. A. (2019). Effect of nozzle pressure ratio and control jets location to control base pressure in suddenly expanded flows. *Journal of Applied Fluid Mechanics*, 12(4), 1127–1135. https://doi.org/10.29252/jafm.12.04.29495

Rakhsha, S., Rajabi Zargarabadi, M., & Saedodin, S. (2023). The effect of nozzle geometry on the flow and heat transfer of pulsed impinging jet on the concave surface. *International Journal of Thermal Sciences*, 184, 107925. https://doi.org/10.1016/j.ijthermalsci.2022.107925

Salimi, M. R., Askari, R., & Hasani, M. (2022). Computational investigation of effects of side-injection geometry on thrust-vectoring performance in a fuel-injected dual throat nozzle. *Journal of Applied Fluid Mechanics*, 15(4), 1137–1153. https://doi.org/10.47176/jafm.15.04.33354

Shyji, S., Deepu, M., Kumar, N. A., & Jayachandran, T. (2017). Numerical studies on thrust augmentation in high area ratio rocket nozzles by secondary injection. *Journal of Applied Fluid Mechanics*, 10(6), 1605–1614. https://doi.org/10.29252/jafm.73.245.27309

Yaravintelimath, A., B. N., R., & A. Moríñigo, J. (2016). Numerical prediction of nozzle flow separation: Issue of turbulence modeling. *Aerospace Science and Technology*, 50, 31–43. https://doi.org/10.1016/j.ast.2015.12.016

Yu, K., Xu, J., Lv, Z., & Song, G. (2019). Inverse design methodology on a single expansion ramp nozzle for scramjets. *Aerospace Science and Technology*, 92, 9–19. https://doi.org/10.1016/j.ast.2019.05.054

Yu, Y. (2020). Over-expanded separation transitions of single expansion ramp nozzle in the accelerating and decelerating processes. *Aerospace Science and Technology*, 98, 105674. https://doi.org/10.1016/j.ast.2019.105674

Yu, Y., Xu, J., Mo, J., & Wang, M. (2014a). Numerical investigation of separation pattern and separation pattern transition in overexpanded single expansion ramp nozzle. *The Aeronautical Journal*, 118(1202), 399–424. Cambridge Core. https://doi.org/10.1017/S0001924000009192

Yu, y., xu, j., mo, j., & wang, m. (2014b). Principal parameters in flow separation patterns of over-expanded single expansion RAMP nozzle. *Engineering Applications of Computational Fluid Mechanics*, 8(2), 274–288. https://doi.org/10.1080/19942060.2014.11015513

Yu, Y., Xu, J., Yu, K., & Mo, J. (2015). Unsteady transitions of separation patterns in single expansion ramp nozzle. *Shock Waves*, 25(6), 623–633. https://doi.org/10.1007/s00193-015-0595-y

Zang, B., U S, V., & New, T. H. D. (2017). *OpenFOAM based numerical simulation study of an underexpanded supersonic jet. 55th AIAA Aerospace Sciences Meeting*. American Institute of Aeronautics and Astronautics. https://doi.org/10.2514/6.2017-0747

Zhou, L., & Wang, Z. (2019). Numerical investigation on the three-dimensional flowfield in the single expansion ramp nozzle with passive cavity flow control. *Journal of Applied Fluid Mechanics*, 12(4), 1115–1126. https://doi.org/10.29252/jafm.12.04.29320